RESEARCH ARTICLE| APRIL 01, 2025

Unusual sulfide-rich magmatic apatite crystals from >2.7 Ga Abitibi Greenstone Belt, Canada

Meng, X., Mole, D.R., **Simon, A.C.**, Mao, J., Kontak, D.J., Jugo, P.J., Kleinsasser, J.
Author and Article Information

American Mineralogist (2025) 110 (4): 622–629.
https://doi.org/10.2138/am-2024-9387

Abstract

Sodic volcano-plutonic terranes in the Archean can be well preserved, but why oxidized S-rich sodic magmas and porphyry-type Cu-Au deposits are so rare remains poorly understood. Here we addressed this issue by measuring the S concentration and $S^{6+}/\Sigma S$ ratio of primary apatite grains in >2.7 Ga felsic volcanic rocks from the well-characterized Neoarchean Abitibi Greenstone Belt of the Superior Province, Canada. Whereas apatite grains in most samples contain low-S concentrations (<0.01 wt%, n = 24), a few apatite samples are S-rich (0.14 ± 0.03 wt%, 1σ) and have low-$S^{6+}/\Sigma S$ ratios (0.56 ± 0.17; 1σ, n = 4). Samples with S-poor apatite have variable whole-rock La/Yb ratios (generally <30) and zircon 10 000*(Eu/Eu*)/Yb ratios of 11 ± 8 (1σ), which may be products of plume-driven or over-thickened crustal melting. In contrast, the samples with S-rich apatite have elevated La/Yb ratios of 49 ± 15 (1σ), zircon 10 000*(Eu/Eu_N*)/Yb ratios of 26 ± 7 (1σ), and zircon $\delta^{18}O$ values of 5.8 ± 0.1 ‰ (1σ), consistent with a deep, hydrous and homogeneous mantle-like source for the melts dominated by amphibole ± garnet fractionation that is reminiscent of subduction-like process. These are the first reported results documenting the predominant accommodation of relatively reduced S in S-rich apatite grains crystallized from terrestrial silicate melts, possibly reflecting slight oxidation associated with the hydration of Neoarchean mantle and crystal fractionation over the magma evolution. The more common S-poor apatite data suggest that suppressed oxidation of the parental sodic magmas led to weak S emission from Earth's interior to its evolving surface, explaining the rarity of porphyry-type Cu deposits in >2.7 Ga Archean sodic volcano-plutonic terranes.

Neoarchean, apatite, oxidation state, melt S, porphyry Cu deposit

Introduction

Subduction zones are the primary loci for chemical exchange among the atmosphere, ocean, lithosphere, and mantle, whereby subduction of hydrated oceanic crust and its sedimentary veneer leads to flux melting of the overlying mantle wedge and generation of arc plutonism and volcanism (Richards 2011). One important consequence of this complex sequence of mass transfer events is the formation of magmatic-hydrothermal ore deposits of the porphyry-type enriched in Cu ± Au ± Mo (Sillitoe 2010; Richards 2011; Audétat and Simon 2012). Petrological and geochemical proxies suggest that subduction-like processes may have operated since 3.0 Ga or earlier (Dhuime et al. 2012), but their extent and duration were likely limited due to the low rheological strength of subducting slabs in a hotter, melt-rich Archean mantle (Sizova et al. 2010; Moyen and van Hunen 2012; Laurent et al. 2014). Oxidized S-rich magmas have recently been identified to correlate with subduction events during the later stages of Archean cratonization in the southeastern Superior Province (<2.7 Ga; Meng et al. 2022). Prior to the later stages of Archean cratonization (>2.7 Ga of the southeastern Superior Province), short-term episodic proto-subduction (~5 Myr) is suggested to have operated based on evidence from whole-rock geochemistry and numerical modeling (Wyman and Kerrich 2009; Moyen and van Hunen 2012). However, it remains unclear as to whether oxidized S-rich sodic magmas and porphyry Cu deposits could have formed before ~2.7 Ga in the Archean.

In this study, we investigated the redox state of sodic magmas formed between ~2750–2695 Ma in the Neoarchean Abitibi Greenstone Belt of the southeastern Superior Province (Fig. 1a) (Mole et al. 2021; Meng et al. 2021a, 2022). This belt comprises arc-like, calc-alkaline-dominated volcanic sequences intercalated with dominantly tholeiitic ± komatiitic assemblages that formed as a part of the assembly of volcano-plutonic terranes from ~2750–2695 Ma prior to interpreted subduction-collision since ~2695 Ma (Figs. 1a and 1b) (Thurston et al. 2008; Beakhouse 2011; Meng et al. 2021a; Mole et al. 2021). We measured the sulfur (S) concentration and relative abundances of S^{6+}, S^{4+}, and S^{2-} in apatite [$Ca_5(PO_4)_3(F,OH,Cl)$], of which the S is incorporated during apatite crystallization from silicate melts (Kim et al. 2022) that are faithfully preserved due to being armored in zircon. Previous studies reported low-$S^{6+}/\Sigma S$ ratios in magmatic apatite grains from the lunar basalts and ~2.35 Ga Na-rich tonalite-trondhjemite-granite (TTG), but the S concentrations in these apatite grains are generally low (Brounce et al. 2019; Moreira et al. 2023). In contrast, apatites with high-S concentrations but negligible S^{6+} and dominant S^{4+} and S^{2-} have only been reported where hydrothermal replacement processes are evident (Sadove et al. 2019). The results presented here reveal, instead, the rare presence of pristine S-rich apatite with relatively low $S^{6+}/\Sigma S$ ratios. Our results suggest, therefore, that the rarity of porphyry-type Cu deposits in well-preserved Archean volcano-plutonic terranes might be attributed to the limited extent and duration of the proto-subduction process with low productivity of oxidized S-rich arc magmas.

Figure 1.

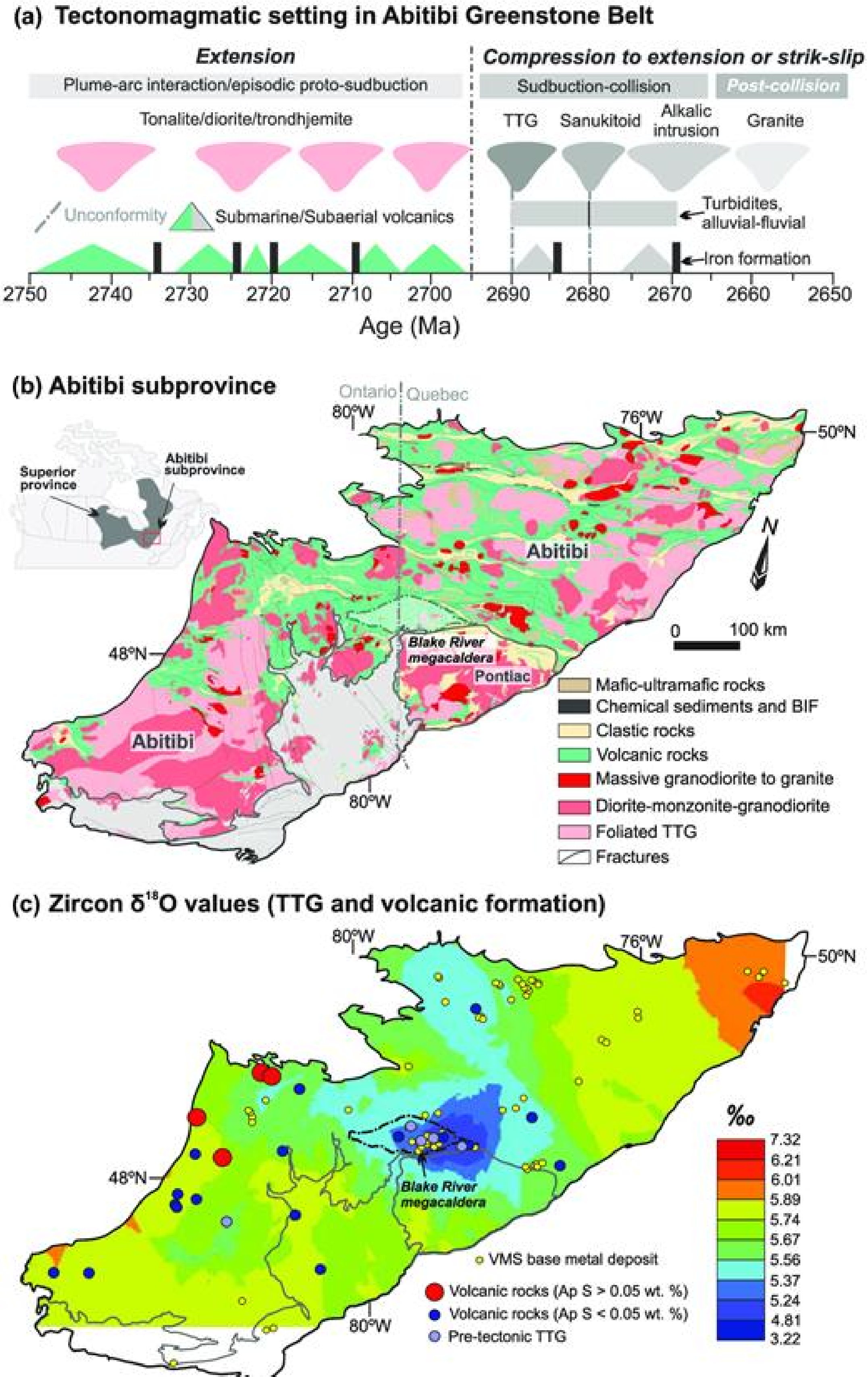

(a) Tectonomagmatic setting in Abitibi Greenstone Belt
Extension
Compression to extension or strik-slip
Plume-arc interaction/episodic proto-sudbuction
Sudbuction-collision
Post-collision
Tonalite/diorite/trondhjemite
TTG
Sanukitoid
Alkalic intrusion
Granite
Unconformity
Submarine/Subaerial volcanics
Turbidites, alluvial-fluvial
Iron formation
2750 2740 2730 2720 2710 2700 2690 2680 2670 2660 2650
Age (Ma)
(b) Abitibi subprovince
Ontario
Quebec
80°W
76°W
50°N
48°N
Superior province
Abitibi subprovince
Abitibi
N
0 100 km
Blake River megacaldera
Pontiac
Mafic-ultramafic rocks
Chemical sediments and BIF
Clastic rocks
Volcanic rocks
Massive granodiorite to granite
Diorite-monzonite-granodiorite
Foliated TTG
Fractures
(c) Zircon δ18O values (TTG and volcanic formation)
80°W
76°W
50°N
48°N
‰
7.32
6.21
6.01
5.89
5.74
5.67
5.56
5.37
5.24
4.81
3.22
Blake River megacaldera
VMS base metal deposit
Volcanic rocks (Ap S > 0.05 wt. %)
Volcanic rocks (Ap S < 0.05 wt. %)
Pre-tectonic TTG

View largeDownload slide

The tectonomagmatic setting and geological map of the Abitibi Greenstone Belt in the southeastern Superior Province, along with the spatial distribution of samples with measured zircon $\delta^{18}O$ values. (**a**) Tectonomagmatic setting (Meng et al. 2021a and references therein); (**b**) lithology (Montsion et al. 2018); (**c**) zircon $\delta^{18}O$ isotopic value [reprocessed with the previously published data sets from Mole et al. (2021)]. (Color online.)

Samples and Methods

The Neoarchean Abitibi Greenstone Belt comprises ~2.75–2.67 Ga east-trending volcano-plutonic assemblages that preserve the following magmatic record: (1) pre-tectonic sodic volcanic rocks and the tonalite-trondhjemite-diorite thought to have formed from "plume-arc" interaction or episodic short-term subduction; (2) early syn-tectonic tonalite-granodiorite and minor volcanic rocks derived from melting of subducted slabs; (3) syn- to late-tectonic sanukitoid suites (sensu lato); and (4) late-tectonic alkalic rocks (i.e., syenite suites) derived from a metasomatized mantle (Percival 2007; Thurston et al. 2008; Beakhouse 2011; Dubé and Mercier-Langevin 2020; Meng et al. 2021a; Mole et al. 2021). The syn- to late-tectonic sodic and potassic rocks that are interpreted to form in subduction-collision settings contain S-rich apatite grains with high-$S^{6+}/\Sigma S$ ratios, reflecting their oxidized S-rich feature of the magmas (Fig. 1a) (Meng et al. 2022). In comparison, the pre-tectonic (i.e., pre-deformation, foliated) sodic volcano-plutonic rocks are of significant interest because they are much more abundant, with some interpreted to have formed in a short-term episodic subduction setting (Wyman and Kerrich 2009; Moyen and van Hunen 2012).

Twenty-eight zircon separate samples of pre-tectonic (i.e., >2695 Ma) volcanic rocks of dacitic to rhyolitic composition were previously collected from the Abitibi Greenstone Belt (Online Materials[1] Table S1). These samples yielded narrow ranges of zircon εHf(t) and $\delta^{18}O$ values, based on our previous studies (i.e.,+3.1 to +4.9 and 4.2 to 6.2‰ respectively; Fig. 1c; Online Materials[1] Table S1) (Mole et al. 2021). We defined "arc-like" features as the enrichment of fluid-mobile elements (e.g., large-ion lithophile, U, and light rare earth elements [LREE]) and relative depletion of high field strength elements (e.g., Nb, Y, heavy rare earth elements [HREE]) (Richards 2011), which importantly can be recorded in zircon geochemistry (Grimes et al. 2015), as discussed below. These inferred arc-like rocks are distinguished by their high-U_i/Nb ratios of ≥40 from the mantle-derived magmas with U_i/Nb ratios of <40 using the previously proposed discrimination criteria (Grimes et al. 2015; Drabon et al. 2021), in which U_i represents the initial U concentrations in the zircon grains at the time of crystallization (Online Materials[1] Table S1).

Apatite inclusions in the mounted zircon grains used in Mole et al. (2021) were identified using a scanning electron microscope equipped with an energy-dispersive spectrometer (SEM-EDS) at Laurentian University (Sudbury, Canada). The S concentration and peak integrated areas of S^{6+}, S^{4+}, and S^{2-} in primary apatite inclusions were measured using an electron microprobe analyzer (EMPA) in the GeoLabs of the Ontario Geological Survey (Sudbury, Canada) and synchrotron-based micro-X-ray absorption near-edge structure spectroscopy (μ-XANES) at S *K*-edge at Advanced Photon Sources (Illinois, U.S.A.). The archived samples for representative volcanic rocks were reused for lithogeochemical analyses at Australian Laboratory Services (ALS, Vancouver, Canada). Details of the methods for EMPA, μ-XANES, and whole-rock geochemistry are provided in Online Materials[1].

Results

The monophase, equant to sub-equant apatite inclusions hosted in zircon grains with oscillatory or sector zoning were divided into two groups based on their S concentration (Table 1; Fig. 2). Group-I apatite grains yielded S concentrations of 0.14 ± 0.03 wt% and $S^{6+}/\Sigma S$ ratios of 0.56 ± 0.17 (1σ; Tables 1 and 2; Fig. 2), while Group-I whole rock samples have La/Yb ratios of 49 ± 15 (1σ), zircon 1000·(Eu/Eu*)/Yb ratios of 26 ± 7, and mantle-like zircon $\delta^{18}O$ isotopic values of 5.8 ± 0.1‰ (1σ; Table 1; Fig. 2). In contrast, Group-II apatite grains yielded S contents of <0.01 wt%, which incidentally, were too low for XANES to measure the abundances of S^{6+}, S^{4+}, and S^{2-}. For these Group-II samples, the whole-rock samples hosting Group-II apatite yielded variable zircon $\delta^{18}O$ values of 4.0–6.5 ‰, as well as La/Yb ratios and zircon 1000·(Eu/Eu*)/Yb ratios that skew to low values of <30 (except for one sample with a ratio of 49) and 11 ± 8, respectively (1σ; Table 1; Online Materials[1] Tables S1 and S2; Fig. 2).

Table 1.

Information for representative pre-tectonic volcanic samples from the Abitibi Greenstone Belt, Canada

Sample no.	Rock type	Zircon U-Pb age[a]	Apatite		Zircon[b]						Whole-rock
			S (wt%)	1σ	$\delta^{18}O$ (‰)	1σ	10000·(Eu/Eu*)/Yb	1σ	ΔFMQ	1σ	La/Yb ratio
Samples with high-S apatite and arc-like zircon U_i/Nb ratios of ≥40											
93HNB-208	Volcanic tuff	2730 ± 1.0	0.171	0.00	5.9	0.3	27.9	9.4	0.83	0.60	N/A

Sample no.	**Rock type**	**Zircon U-Pb age[a]**	**Apatite**		**Zircon[b]**						**Whole-rock**
			S (wt%)	**1σ**	**$\delta^{18}O$ (‰)**	**1σ**	**10000·(Eu/Eu*)/Yb**	**1σ**	**ΔFMQ**	**1σ**	**La/Yb ratio**
				68							
96JAA-041	Felsic volcanic	2718 ± 2.3	0.123	0.053	5.8	0.1	30.6	6.1	0.84	0.38	38
96JAA-011	Felsic volcanic	2694 ± 4.5	0.145	0.084	5.9	0.1	29.9	9.5	2.28	0.21	59
06-BRB-246	Quartz-phyric volcanic	2722 ± 1.7	0.109	0.000	5.7	0.0	16.3	4.4	2.22	0.53	N/A
Average			**0.14**		**5.8**		**26.2**		**1.5**		**49**

Sample no.	Rock type	Zircon U-Pb age[a]	Apatite		Zircon[b]						Whole-rock
			S (wt%)	1σ	δ^{18}O (‰)	1σ	10000·(Eu/Eu*)/Yb	1σ	ΔFMQ	1σ	La/Yb ratio
1σ			**0.03**		**0.1**		**6.7**		**0.8**		**15**
Samples with low-S apatite and arc-like zircon U_i/Nb ratios of ≥40											
92HNB-0083	Felsic Lapilli tuff	2701 ± 2.3	0.004[BDL]	0.002	5.7	0.2	12.9	4.9	0.19	0.50	N/A
94HNB0059	Rhyolite lapilli tuff	2735 ± 6.0	0.008[BDL]	0.002	4.9	0.2	16.0	3.8	0.04	0.54	N/A
96JAA-086	Felsic Lapilli tuff	2710 ± 1.9	0.011[BDL]	0.001	5.5	0.2	4.7	3.0	–0.65	0.56	10

Sample no.	Rock type	Zircon U-Pb age[a]	Apatite		Zircon[b]						Whole-rock
			S (wt%)	1σ	$\delta^{18}O$ (‰)	1σ	10000·(Eu/Eu*)/Yb	1σ	ΔFMQ	1σ	La/Yb ratio
98JAA-0019	Felsic tuff breccia	2717 ± 1.7	0.000 BDL	N/A	5.5	0.1	14.0	4.3	0.08	0.43	20
C-82-8	Dacite tuff	2701 ± 2.0	0.014	0.002	5.2	0.1	23.5	4.6	0.87	0.37	49
93HNB-087A	Felsic lapilli tuff	2731 ± 2.0	0.039	0.033	5.6	0.6	17.6	5.7	0.09	0.34	N/A
C88-17	Rhyolite	2725 ± 1.0	0.004 BDL	0.002	5.5	0.2	5.3	1.1	−0.37	0.18	10

Sample no.	Rock type	Zircon U-Pb age[a]	Apatite		Zircon[b]						Whole-rock
			S (wt %)	1σ	$\delta^{18}O$ (‰)	1σ	10000·(Eu/Eu*)/Yb	1σ	ΔFMQ	1σ	La/Yb ratio
93HNB-0205B	Felsic tuff	2724 ± 1.0	0.012	0.009	5.7	0.2	23.4	8.7	–0.18	0.30	N/A
SGNO2000-07	Felsic tuff	2721 ± 0.8	0.000 BDL	N/A	5.7	0.1	16.6	6.0	–0.22	0.15	18
94HNB-0281	Rhyolite	2718 ± 2.0	0.000 BDL	N/A	5.1	0.3	6.2	7.2	–0.38	0.57	N/A
C-82-7	Dacitic flow	2711 ± 3.0	0.008 BDL	0.000	5.8	0.1	12.9	0.8	0.34	1.12	N/A

Sample no.	Rock type	Zircon U-Pb age[a]	Apatite		Zircon[b]						Whole-rock
			S (wt%)	1σ	$\delta^{18}O$ (‰)	1σ	10000·(Eu/Eu*)/Yb	1σ	ΔFMQ	1σ	La/Yb ratio
94HNB-0115	Feldspar-quartz tuff	2707 ± 1.0	0.006 BDL	0.006	5.5	0.3	6.1	1.7	−0.03	0.33	N/A
96TB082	Dacite breccia	2705 ± 1.5	0.012	0.002	5.7	0.1	9.8	2.9	−0.07	0.63	N/A
LAPL-146-2000	Rhyodacite	2698 ± 0.8	0.004 BDL	0.001	4.8	0.2	3.2	0.5	0.33	0.40	17
03ASP0179.1.1	Rhyolite	2697 ± 1.3	0.004 BDL	0.003	4.7	0.2	4.1	2.8	−0.87	0.54	5

Sample no.	Rock type	Zircon U-Pb age[a]	Apatite		Zircon[b]						Whole-rock
			S (wt%)	1σ	$\delta^{18}O$ (‰)	1σ	10000·(Eu/Eu*)/Yb	1σ	ΔFMQ	1σ	La/Yb ratio
95HNB-0273	Felsic volcanic	2695 ± 2.0	0.014	0.000	6.2	0.2	24.7	6.3	0.89	0.35	N/A
SGNO-Bousquet 2	Rhyolite	2698 ± 1.0	0.000 BDL	0.000	4.6	0.2	3.7	2.0	N/A	N/A	26
SGNO99-10	Rhyolite	2703 ± 0.9	0.006 BDL	0.000	5.2	0.2	1.3	0.4	N/A	N/A	3
94HNB-267	Quartz-phyric volcanic	2715 ± 2.0	0.007 BDL	0.010	5.7	0.2	N/A	N/A	N/A	N/A	N/A

Sample no.	Rock type	Zircon U-Pb age[a]	Apatite		Zircon[b]						Whole-rock
			S (wt%)	1σ	$\delta^{18}O$ (‰)	1σ	10000·(Eu/Eu*)/Yb	1σ	ΔFMQ	1σ	La/Yb ratio
C83-16	Dacitic tuff	2729 ± 3.0	0.0007 BDL	0.000	6.1	0.2	N/A	N/A	N/A	N/A	N/A
Average			**0.008**		**5.4**		**11.4**		**0.0**		**18**
1σ			**0.009**		**0.4**		**7.6**		**0.5**		**14**
Samples with low-S apatite and low-zircon U_i/Nb ratios of <40											
R-16	Rhyolite tuff	2706 ± 2.0	0.0010 BDL	0.012	5.7	0.2	2.470	0.750	1.19	0.56	

Sample no.	Rock type	Zircon U-Pb age[a]	Apatite		Zircon[b]						Whole-rock
			S (wt%)	1σ	$\delta^{18}O$ (‰)	1σ	10 000· (Eu/Eu*)/Yb	1σ	ΔFMQ	1σ	La/Yb ratio
SGNO-2005-02	Dacite tuff	2706 ± 3.3	0.003 BDL	0.003	5.3	0.3	6.464	5.138	−0.44	0.41	
SGNO 2001-07	Rhyolite	2697 ± 0.8	0.000 BDL	N/A	4.2	0.1	2.168	0.545	0.91	0.42	
SGNO 2000-08	Rhyolite	2696 ± 1.1	0.003 BDL	0.000	4.3	0.1	2.409	0.809	1.20	0.34	10

Notes: The filtered trace element data were used for calculating 10 000 · (Eu/Eu*)/Yb and ΔFMQ values (Loucks et al. 2020; Loucks and Fiorentini 2023). Abbreviations: BDL = below the detection limit (0.012 wt% for EMPA apatite S concentration).

[a] The zircon U-Pb ages of the studied volcanic rocks were analyzed using ID-TIMS and LA-MC-ICP-MS methods [see the compilation in Mole et al. (2021)]. Error type is 2 standard errors.

[b] Zircon O isotopes and trace element data were filtered from the original data set in Mole et al. (2021) using the following criteria: (1) La content <1 ppm; (2) LREE Index (LREE-I) = (Dy/Nd) + (Dy/Sm) >10; (3) Ti content > detection limit and <50 ppm; (4) age discordance <10% (Lu 2016; Bell et al. 2016; Meng et al. 2021a).

View large

Figure 2.

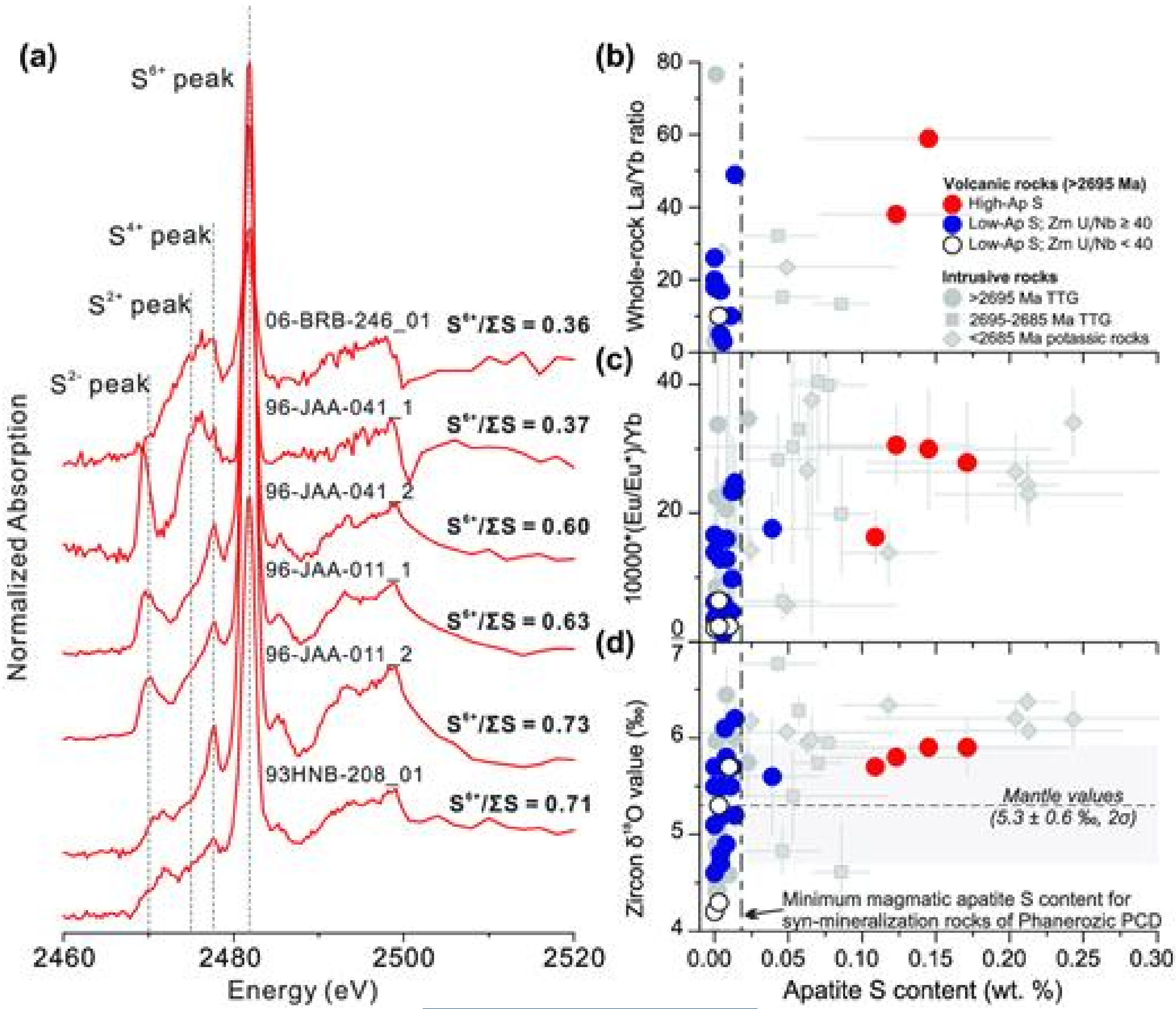

View largeDownload slide

The normalized μ-XANES spectra at S *K*-edge for the S-rich apatite grains as well as the analyzed apatite S concentration vs. (**b**) whole-rock La/Yb ratios, (**c**) zircon 10 000 · (Eu/Eu*)/Yb ratios (a proxy of magma hydration state, see Loucks and Fiorentini 2023), and (**d**) zircon $\delta^{18}O$ values from the >2695 Ma volcanic rocks in the Abitibi Greenstone Belt (from Mole et al. 2021). Group-I and Group-II apatite grains and the host rocks are shown in red and blue, respectively. The mantle value for zircon O isotopes is 5.3 ± 0.3 wt% (1σ; Valley et al. 1998). The apatite data for intrusive rocks were reported by Meng et al. (2022). The S concentrations in primary apatite grains from syn-mineralization intrusive rocks for porphyry Cu deposits are compiled in Online Materials[1] Table S5. Note that the zircon $\delta^{18}O$ values and 10 000·(Eu/Eu*)/Yb ratios are recalculated based on data sets reported by Mole et al. (2021). Error bars represent standard deviation. (Color online.)

Table 2.

Estimates of ΔFMQ values and melt S concentrations for the samples with S-rich apatite grains from Abitibi Greenstone Belt, Canada

Sample no.	**Rock type**	**$S^{6+}/\Sigma S$**	**1σ**	**ΔFMQ (S-in-apatite oxybarometer)**						**Model melt S content (Meng et al. 2021b)**					
				***P-T* un-corrected**	**1σ**	**892 °C 1 atm**	**1σ**	**892 °C 700 MPa**	**1σ**	**843 °C 1 atm**	**843 °C 700 MPa**	**892 °C 1 atm**	**892 °C 700 MPa**	**941 °C 1 atm**	**941 °C 700 MPa**
93HNB-208	Volcanic tuff	0.71		0.60		0.94	0.25	1.41	0.25	0.20	0.12	0.34	0.21	0.34	0.21
96JAA-0	Felsic volca	0.49	0.16	0.39	0.15	0.73	0.40	1.19	0.40	0.18	0.11	0.31	0.19	0.30	0.19

Sample no.	Rock type	$S^{6+}/\Sigma S$	1σ	ΔFMQ (S-in-apatite oxybarometer)						Model melt S content (Meng et al. 2021b)					
				P-*T* un-corrected	1σ	892 °C 1 atm	1σ	892 °C 700 MPa	1σ	843 °C 1 atm	843 °C 700 MPa	892 °C 1 atm	892 °C 700 MPa	941 °C 1 atm	941 °C 700 MPa
41	nic														
96JAA-011	Felsic volcanic	0.68	0.07	0.57	0.07	0.91	0.32	1.38	0.32	0.17	0.11	0.30	0.19	0.29	0.18
06-BRB-246	Quartz-phyric volc	0.36		0.27		0.61	0.25	1.07	0.25	0.18	0.11	0.31	0.19	0.30	0.19

Sample no.	Rock type	$S^{6+}/\Sigma S$	1σ	ΔFMQ (S-in-apatite oxybarometer)						Model melt S content ([Meng et al. 2021b](#))					
				P-*T* un-corrected	1σ	892 °C 1 atm	1σ	892 °C 700 MPa	1σ	843 °C 1 atm	843 °C 700 MPa	892 °C 1 atm	892 °C 700 MPa	941 °C 1 atm	941 °C 700 MPa
	anic														
Average		0.56		0.46		0.80		1.26		0.18	0.11	0.31	0.19	0.31	0.19
s.d.		0.17		0.16		0.16		0.16		0.01	0.01	0.02	0.01	0.02	0.01

Notes: The ΔFMQ values are estimated using the S-in-apatite oxybarometer (Konecke et al. 2019), whereas the melt S concentrations are estimated using the model for the partitioning of S between apatite and melt using existing apatite/melt partition coefficient values as function of magmatic fO2 and temperature (Parat and Holtz 2004; Konecke et al. 2019; Meng et al. 2021b). The zircon-hosted apatite crystals from the volcanic rocks are assumed to crystallize at pressure over a range from that for the pre-tectonic TTG batholith (300–700 MPa and locally 100 MPa; Beakhouse et al. 2005, 2011) to near-atmospheric pressure. The modeled range of temperature (892 ± 49 °C; 1σ, n = 1372) is estimated using the apatite saturation thermometer (Piccoli and Candela 2002). The standard deviations for the corrected magmatic fO2 in ΔFMQ involve the intra-sample standard deviation and those derived for the pressure and temperature estimation. For simplicity, the standard deviation of intra-sample apatite $S^{6+}/\Sigma S$ ratios is not considered in estimating the melt S concentration. See details of the relevant methods in Online Materials[1].

View large

The $S^{6+}/\Sigma S$ ratio in apatite varies systematically with the oxygen fugacity (fO2) of the magmatic system as demonstrated experimentally by Konecke et al. (2019), whereas the S concentration in apatite is a function of magmatic fO2, crystallization temperature, and S concentration of the melt (Parat and Holtz 2004; Konecke et al. 2019; Meng et al. 2021b). Magmatic fO2, expressed here as ΔFMQ values, were estimated using the calculated $S^{6+}/\Sigma S$ ratios and the *P*-*T*-corrected S-in-apatite oxybarometer (Online Materials[1]). The results yielded a relatively low average ΔFMQ value of 0.80 ± 0.16 to 1.26 ± 0.16 (1σ) for Group-I apatite (Table 2). A model for the partitioning of S between apatite and melt (DSap/m) using existing apatite/melt partition coefficient values as a function of magmatic fO2 and temperature (Meng et al. 2021b) was used to calculate a model S concentration of 0.11–0.34 wt% in the silicate melt at the time of crystallization of Group-I apatite (Table 2).

Discussion

Formation of unusual sulfide-rich apatite

Historic studies used a mass-balance approach with EPMA-determined concentrations of S and other cations in apatite, as required for coupled substitutions, to hypothesize that S^{6+} is the dominant S species in the apatite structure (Konecke et al. 2019 and references therein). However, recent studies using S-μ-XANES demonstrate that the multiple oxidation states of S, including S^{6+}, S^{4+}, S^{0}, S^{1-}, and S^{2-}, are instead incorporated into apatite crystallized from hydrothermal fluids (Sadove et al. 2019), hosted in lunar basalts (Brounce et al. 2019), as well as those formed in both experimental and terrestrial silicate melts (Konecke et al. 2019; Kim et al. 2022; Meng et al. 2021a, 2021b, 2022). Previous experimental and empirical studies for magmatic systems generally reported high-$S^{6+}/\Sigma S$ ratios in apatite with a strong positive correlation between their $S^{6+}/\Sigma S$ ratio and S contents, in agreement with experimental data for silicate melts that document higher concentrations of S^{6+} than S^{2-} coupled with high fO2 (Konecke et al. 2019; Tassara et al. 2020; Meng et al. 2021a, 2021b, 2022; Moreira et al. 2023). In contrast to the previous studies suggesting covariance of $S^{6+}/\Sigma S$ ratio and S concentrations in magmatic apatite, the S-μ-XANES data reported here are the first to our knowledge to reveal that S-rich igneous apatite with low-$S^{6+}/\Sigma S$ ratios of ~0.5 crystallized under fO2 conditions of ~ΔFMQ +1 where the $S^{6+}/\Sigma S$ ratio of the silicate melt is ~0.1 (Kleinsasser et al. 2022, 2024). Compared to silicate melt, apatite preferentially incorporates sulfate (S^{6+}) rather than the reduced-intermediate redox state of S (e.g., S^{2-}, S^{4+}, S^{1+}) (Konecke et al. 2019). The range of the model S concentration in the melts overlaps the maximum values of S content at sulfide saturation (SCSS) for basaltic to dacitic silicate melts (0.1–0.2 wt%) (Kleinsasser et al. 2022). Hence, the $S^{6+}/\Sigma S$ ratio of ~0.5 and high-S concentration of apatite in Group-I samples can only be explained by the crystallization of apatite from sulfide-saturated silicate melts where the SCSS is at its maximum value. This inferred sulfide saturation at the time of apatite crystallization is preserved in the form of pyrrhotite ($Fe_{0.93}S$; based on EDS data) inclusion exposed in zircon-hosted apatite grains in the Group-I sample (sample 93HNB-208; Online Materials[1] Fig. S1g).

Origin of the >2.7 Ga arc-like magmas

The high-zircon U_i/Nb ratio of ≥40 is interpreted to reflect fluid-mobile element enrichment in the source region and/or relative depletion of immobile elements during the crystal fractionation (e.g., garnet, amphibole) (Grimes et al. 2015; Drabon et al. 2021). These samples can be grouped with respect to the apatite S concentrations. The high whole-rock La/Yb and zircon (Eu/Eu*)/Yb ratios for Group-I samples reflect a deep source and hydrous state for the sodic magmas (Moyen 2009; Loucks and Fiorentini 2023), which may be formed from either partial melting of subducting slab or metasomatized mantle (Moyen and van Hunen 2012), remelting of thickened hydrated mafic crust (Bédard 2018; Mole et al. 2021), or plagioclase ± amphibole fractionation of parental tonalitic liquids from basalt melting (Laurent et al. 2020). The slightly elevated ΔFMQ value of +0.7–1.4 estimated using the S-in-apatite oxybarometer for Group-I samples is more consistent with the former two models because: (1) slab-derived fluids are capable of oxidizing the mantle in the Archean (Meng et al. 2022); (2) magmas can be further oxidized during fluid-undersaturated magma differentiation at Moho-vicinity depths (Loucks and Fiorentini 2023); or (3) crystallization of significant amounts of garnet slightly increases reduced magmas in the fO2 value by ≤0.8 log unit (Tang et al. 2018, Holycross and Cottrell 2023). The high 1000 · (Eu/Eu*)/Yb ratios of the zircon grains indicate suppression of Eu depletion in plagioclase-undersaturated silicate melt or Yb depletion due to hornblende crystallization during zircon precipitation (Loucks and Fiorentini 2023). The crystallization of hydrous amphibole, as well as suppression of anhydrous plagioclase crystallization, indicate elevated H_2O concentrations in the magmas. The high 1000·(Eu/Eu*)/Yb ratios with mantle-like O isotopic values, therefore, indicate relatively hydrous magmas formed by hydration of the mantle-like source regions in a subduction-like setting (Fig. 3a), consistent with the previously proposed episodic subduction-like process (Moyen and van Hunen 2012). Fluids released from the subducted slab, without interaction with sediments, plausibly oxidize the mantle source by hydrogen incorporation in the surrounding mantle (e.g., orthopyroxene) coupled with H_2O dissociation (Tollan and Hermann 2019). The estimated S concentration of 0.11–0.34 wt% in the evolved silicate melt represents the lower limit of the S concentration in the parental magmas due to sulfide saturation during magma differentiation. The high-S concentration in the parental magmas with limited oxidation state could be attributed in part to the active upwelling of sulfide-saturated Archean mantle during the frequent slab breakoff or contamination by a lower crustal reservoir enriched in reduced S (e.g., mafic cumulate).

Figure 3.

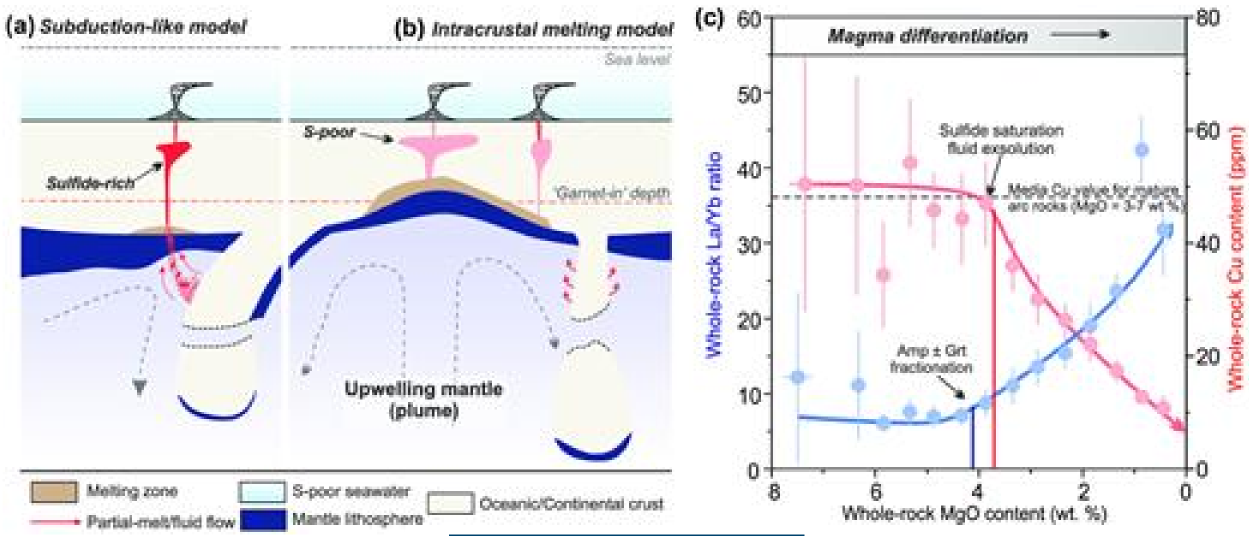

Schematic diagrams (**a** and **b**) illustrating the tectonomagmatic models for the Abitibi Greenstone Belt of the southeastern Superior Province with (**c**) whole-rock MgO contents vs. La/Yb ratio and Cu concentration (n = 2091 and 1873, respectively) for the sodic magmas. The symbols in **c** represent the average value with 2 standard errors. Note that the whole-rock geochemistry data were compiled by Mole et al. (2021) and are reprocessed following the method in Online Materials[1]. The data plotted in panel **c** were filtered using criteria as follows: (1) SiO_2 <75 wt%; (2) loss on ignition (LOI) ≤2 wt%; (3) K_2O/Na_2O <0.6 (Online Materials[1] Table S4). (Color Online.)

The observed increase in magmatic fO2 values with further magma cooling, as estimated from the zircon oxybarometer (Online Materials[1] Fig. S2), may be attributed to: (1) either the increase in the Fe^{3+}/Fe^{2+} ratio of the melt during fluid-unsaturated fractionation of ferromagnesian silicates (Ulmer et al. 2018); or (2) decompression-driven exsolution of hydrothermal fluids (Bell and Simon 2011; Loucks and Fiorentini 2023). Exsolution of SO_2 from the sulfide-rich magmas would reduce vs. increase the magmatic fO2 (Métrich et al. 2009), so we suggest that the increase in magmatic fO2 with cooling is more consistent with the fractionation of ferromagnesian silicates.

The exceptionally rare occurrence of >2.7 Ga arc-type sodic magmas with high-apatite S concentrations and low-$S^{6+}/\Sigma S$ ratios (Fig. 2) may be interpreted to suggest the aforementioned oxidation process was merely localized and insufficient. In contrast, most of the other arc-like samples (Group-II) yielded relatively low apatite S concentrations, below the detection limit (0.012 wt%), as well as zircon (Eu/Eu*)/Yb ratios and whole-rock La/Yb ratios skewing to lower values. The geochemical features for Group-II samples were more consistent with their derivation from shallow intra-crustal melting of a mafic source or plagioclase ± amphibole differentiation of basalt-derived parental liquids (Fig. 3b), which could explain the relatively dry (as manifested by the generally lower zircon [Eu/Eu*]/Yb ratios) and reduced redox state of the sodic magmas (ΔFMQ value of 0.0 ± 0.5 on average estimated using zircon geochemistry; Table 1).

Ore-forming potential of the >2.7 Ga sodic magmas

Plots of the whole-rock data for the sodic igneous rocks from the Abitibi subprovince (Fig. 3c; Online Materials[1] Table S4) reveal that: (1) less evolved sodic magmas (MgO content >4 wt%; a proxy for magma differentiation) yield Cu concentration of ~50 ppm, which is comparable to Phanerozoic arc magmas (Richards 2015); and (2) with decreasing whole-rock MgO content, the whole-rock La/Yb ratio increases and the concentration of Cu decreases, consistent with loss of Cu to magmatic sulfides during amphibole±garnet-dominated fractionation or by early volatile exsolution (Fig. 3c). Magmatic sulfides in hydrous upper crustal magma reservoirs are thought to be capable of temporarily retaining S and Cu that can subsequently be destabilized by the exsolved magmatic-hydrothermal fluids (Audétat and Simon 2012; Chelle-Michou and Rottier 2021) in tandem with a concomitant increase in magmatic fO2 (Loucks and Fiorentini 2023). We suggest this scenario might have operated locally by considering the rare occurrence of slightly oxidized and S-rich magmas with sulfide-rich apatite grains. In comparison, for most of the relatively dry, reduced pre-tectonic sodic magmas, the S-poor apatite grains may reflect sulfide saturation at a greater depth (e.g., lower crust) and/or the ineffective capacity of many relatively dry sodic magmas to exsolve oxidized S-rich hydrothermal fluids. Because syn-mineralization magmas associated with medium- to large-size porphyry-type Cu deposits typically yielded ΔFMQ values of +1 to +2 and S-bearing apatite grains (S content >0.02 wt%; Fig. 2; Online Materials[1] Table S5), we suggest that the pre-tectonic sodic magmas, including those with arc affinity may have limited, although not totally excluded (e.g., Coté gold; Katz et al. 2021), the formation of porphyry-type Cu deposits in the Archean Greenstone Belt.

Implications

The results presented here demonstrate the presence of S-rich apatite grains with a low-$S^{6+}/\Sigma S$ ratio crystallized from >2.7 Ga slightly oxidized and S-rich terrestrial silicate melts, which may have formed in association with the short-lived proto-subduction in the Neoarchean Abitibi Greenstone Belt. In contrast, most of the >2.7 Ga pre-tectonic arc-like igneous rocks, as classified using zircon U_i/Nb ratios of ≥40, yielded S-poor apatite grains that may reflect relatively reduced or S-poor features of the magmas. The results indicate either local or weak emission of oxidized S from sodic magma reservoirs to the near-surface environment during early Earth's history. These conclusions can explain the rarity of porphyry-type Cu deposits associated with syn-volcanic TTG rocks that were prevalent in >2.7 Ga in the Abitibi Greenstone Belt and possibly in other cratons.

Funding

The research was funded by the National Natural Science Foundation of China (Grant # 41820104010, J.M.), Canada First Research Excellence Fund via Metal Earth (CFREF-2015-00005), U.S. National Science Foundation EAR (Grant # 2233425 and 2214119, A.C.S.), and a start-up research grant from China University of Geosciences (Grant # 3-8-2023-008, X.M.).

Accepted manuscript online July 16, 2024
Manuscript handled by Claire E. Bucholz

Endnote:

1

Deposit item AM-25-49387. Online Materials are free to all readers. Go online, via the table of contents or article view, and find the tab or link for supplemental materials.

Acknowledgments

D. Crabtree is appreciated for his assistance in electron microprobe analysis, and both A. Lanzirotti and M. Newville are thanked for their assistance with the μ-XANES analyses. The Jack Satterley Geochronology Laboratory at the University of Toronto (Ontario, Canada) is thanked for the provision of the rock samples used in this study. This research used synchrotron resources (Sector 13-ID-E) of Advanced Photon Source in Argonne National Laboratory under Contract No. DE-AC02-06CH11357. We sincerely appreciate Claire Bucholz and an anonymous reviewer for their insightful and constructive reviews.

References Cited

1.
Audétat
,
A.
and
Simon
,
A.
(
2012
)
Magmatic controls on porphyry copper genesis
. Society of Economic Geologists
Special Publication
,
16
,
553
–
572
.
Google Scholar

2.
Beakhouse
,
G.P.
(

2011
) The Abitibi Subprovince plutonic record: Tectonic and metallogenic implications.
Ontario Geological Survey
, Open File,
6268
,
1
–
161
.

3.
Beakhouse
,
G.P.
and
Davis
,
D.W
. (
2005
)
Evolution and tectonic significance of intermediate to felsic plutonism associated with the Hemlo greenstone belt, Superior Province, Canada
.
Precambrian Research
,
137
(
1–2
),
61
–
92
.
Google Scholar

4.
Bédard
,
J.H.
(
2018
)

Stagnant lids and mantle overturns: Implications for Archaean tectonics, magma genesis, crustal growth, mantle evolution, and the start of plate tectonics
.
Geoscience Frontiers
,
9
,
19
–
49
, https://doi.org/10.1016/j.gsf.2017.01.005.
Google Scholar

5.
Bell
,
A.S.
and
Simon
,
A.
(
2011
)
Experimental evidence for the alteration of the $Fe^{3+}/\Sigma Fe$ of silicate melt caused by the degassing of chlorine-bearing aqueous volatiles
.
Geology
,
39
,
499
–
502
, https://doi.org/10.1130/G31828.1.
GeoScienceWorld
Google Scholar

6.
Bell
,
E.A.
,
Boehnke

, P., and Harrison, T.M. (2016) Recovering the primary geochemistry of Jack Hills zircons through quantitative estimates of chemical alteration. *Geochimica et Cosmochimica Acta*, 191, 187–202, https://doi.org/10.1016/j.gca.2016.07.016.
Google Scholar

7. Brounce, M., Boyce, J., McCubbin, F.M., Humphreys, J., Reppart, J., Stolper

, E., and Eiler, J. (2019) The oxidation state of sulfur in lunar apatite. *American Mineralogist*, 104, 307–312, https://doi.org/10.2138/am-2019-6804.
GeoScienceWorld
Google Scholar
Crossref

8. Chelle-Michou, C. and Rottier, B. (2021) Transcrustal magmatic controls on the size of porphyry Cu systems: State of knowledge and open questions. *SEG special publications*, 24, 87–

100
.
Google Scholar

9.
Dhuime
,
B.
,
Hawkesworth
,
C.J.
,
Cawood
,
P.A.
, and
Storey
,
C.D.
 (
2012
)
A change in the geodynamics of continental growth 3 billion years ago
.
Science
 ,
335
,
1334
–
1336
, https://doi.org/10.1126/science.1216066.
Google Scholar
Crossref

PubMed

10.
Drabon
,
N.
,
Byerly

, B.L., Byerly, G.R., Wooden, J.L., Keller, C.B., and Lowe, D.R. (2021) Heterogeneous Hadean crust with ambient mantle affinity recorded in detrital zircons of the Green Sandstone Bed, South Africa. *Proceedings of the National Academy of Sciences of the United States of America, 118, e2004370118*, https://doi.org/10.1073/pnas.2004370118.
Google Scholar

11. Dubé, B. and Mercier-Langevin, P. (2020) Gold deposits of the Archean Abitibi Greenstone Belt, Canada. Society of Economic Geologists *Special Publication*,

23, 669–708. Google Scholar

12. Grimes, C.B., Wooden, J.L., Cheadle, M.J., and John, B.E. (2015) “Fingerprinting” tectono-magmatic provenance using trace elements in igneous zircon. *Contributions to Mineralogy and Petrology*, 170, 46, https://doi.org/10.1007/s00410-015-1199-3.
Google Scholar
Crossref

13. Holycross, M. and

Cottrell, E. (2023) Garnet crystallization does not drive oxidation at arcs. *Science*, 380, 506–509, https://doi.org/10.1126/science.ade3418.
Google Scholar
Crossref
PubMed

14. Katz, L.R., Kontak, D.J., Dubé, B., McNicoll, V., Creaser, R., and Petrus,

J.A. (2021) An Archean porphyry-type gold deposit: The Côté Gold Au(-Cu) deposit, Swayze Greenstone Belt, Superior Province, Ontario, Canada. *Economic Geology and the Bulletin of the Society of Economic Geologists* , 116, 47–89, https://doi.org/10.5382/econgeo.4785.
GeoScienceWorld
Google Scholar
Crossref

15. Kim, Y., Konecke, B., Simon, A., Fiege, A., and Becker, U. (2022)

An ab-initio study on the thermodynamics of disulfide, sulfide, and bisulfide incorporation into apatite and the development of a more comprehensive temperature, pressure, pH, and composition-dependent model for ionic substitution in minerals
.
American Mineralogist
,
107
,
1995
–
2007
, https://doi.org/10.2138/am-2022-8250.
GeoScienceWorld
Google Scholar
Crossref

16.
Kleinsasser
,
J.M.
,
Simon
,
A.C.
,
Konecke
,
B.A.
,
Kleinsasser
,
M.J.
,
Beckmann
,
P.
, and
Holtz
,
F.
(
2022
)

Sulfide and sulfate saturation of dacitic melts as a function of oxygen fugacity
.
Geochimica et Cosmochimica Acta
,
326
,
1
–
16
, https://doi.org/10.1016/j.gca.2022.03.032.
Google Scholar
Crossref

17.
Kleinsasser
,
J.
,
Konecke
,
B.A.
,
Simon
,
A.C.
,
Northrup
,
P.
,
Lanzirotti
,
A.
,
Newville
,
M.
,
Borca
,
C.
,
Huthwelker

, T., and Holtz, F. (2024) Sulfur speciation in dacitic melts using X-ray absorption near-edge structure spectroscopy of the S *K*-edge (S-XANES): Consideration of radiation-induced changes and the implications for sulfur in natural arc systems. *American Mineralogist*, 109, 1359–1374, https://doi.org/10.2138/am-2022-8833.
GeoScienceWorld
Google Scholar
Crossref

18. Konecke, B.A., Fiege, A., Simon, A.C., Linsler, S., and Holtz

, F. (2019) An experimental calibration of a sulfur-in-apatite oxybarometer for mafic systems. *Geochimica et Cosmochimica Acta*, 265, 242–258, https://doi.org/10.1016/j.gca.2019.08.044.
Google Scholar
Crossref

19. Laurent, O., Martin, H., Moyen, J.F., and Doucelance, R. (2014) The diversity and evolution of late-Archean granitoids: Evidence for the onset of “modern-style” plate tectonics between 3.0 and 2.5Ga. *Lithos*, 205

, 208 – 235 .
Google Scholar
Crossref

20. Laurent , O. , Björnsen , J. , Wotzlaw , J.F. , Bretscher , S. , Pimenta Silva , M. , Moyen , J.F. , Ulmer , P. , and Bachmann , O. (2020)

Earth's earliest granitoids are crystal-rich magma reservoirs tapped by silicic eruptions
.
Nature Geoscience
,
13
,
163
–
169
, https://doi.org/10.1038/s41561-019-0520-6.
Google Scholar
Crossref

21.
Loucks
,
R.R.
and
Fiorentini
,
M.L.
(
2023
)
Oxidation of magmas during gain and loss of H_2O recorded by trace elements in zircon
.
Earth and Planetary Science Letters
,
622
,
118377
, https://doi.org/10.1016/j.epsl.2023.118377.
Google Scholar
Crossref

22.
Loucks
,
R.R.
,
Fiorentini
,

M.L., and Henríquez, G.J. (2020) New magmatic oxybarometer using trace elements in zircon. *Journal of Petrology*, 61, egaa034, https://doi.org/10.1093/petrology/egaa034.
Google Scholar

23. Lu, Y.J. (2016) Zircon compositions as a pathfinder for porphyry Cu ± Mo ± Au deposits. *Society of Economic Geologists Special Publication*, 19, 329–347.
Google Scholar

24. Meng, X., Richards, J.P., Kontak

,
D.J.
,
Simon
,
A.C.
,
Kleinsasser
,
J.M.
,
Marsh
,
J.H.
,
Stern
,
R.A.
, and
Jugo
,
P.J.
 (
2021a
)
Variable modes of formation for tonalite-trondhjemite-granodiorite-diorite (TTG)-related porphyry-type Cu ± Au deposits in the Neoarchean Southern Abitibi Subprovince (Canada): Evidence from petrochronology and oxybarometry
.
Journal of Petrology
 ,
62
, egab079, https://doi.org/10.1093/petrology/egab079.
Google Scholar

25.
Meng
,
X.
,
Kleinsasser
,
J.M.
,

Richards, J.P., Tapster, S.R., Jugo, P.J., Simon, A.C., Kontak, D.J., Robb, L., Bybee, G.M., Marsh, J.H., and others. (2021b) Oxidized sulfur-rich arc magmas formed porphyry Cu deposits by 1.88 Ga. *Nature Communications*, 12, 2189, https://doi.org/10.1038/s41467-021-22349-z.
Google Scholar
Crossref

PubMed

26.
Meng
,
X.
,
Simon
,
A.C.
,
Kleinsasser
,
J.M.
,
Mole
,
D.R.
,
Kontak
,
D.J.
,
Jugo
,
P.J.
,
Mao
,
J.
, and
Richards
,
J.P.
 (
2022
)
Formation of oxidized sulfur-rich magmas in Neoarchaean subduction zones
.
Nature Geoscience
 ,
15
,

1064–1070, https://doi.org/10.1038/s41561-022-01071-5.
Google Scholar
Crossref

27. Métrich, N., Berry, A.J., O'Neill, H.St.C., and Susini, J. (2009) The oxidation state of sulfur in synthetic and natural glasses determined by X-ray absorption spectroscopy. *Geochimica et Cosmochimica Acta*, 73, 2382–2399, https://doi.org/10.1016/j.gca.2009.01.025.
Google Scholar
Crossref

28. Mole

, D.R., Thurston, P.C., Marsh, J.H., Stern, R.A., Ayer, J.A., Martin, L.A.J., and Lu, Y.J. (2021) The formation of Neoarchean continental crust in the south-east Superior Craton by two distinct geodynamic processes. *Precambrian Research*, 356, 106104, https://doi.org/10.1016/j.precamres.2021.106104.
Google Scholar
Crossref

29. Montsion

,
R.
,
Thurston
,
P.
, and
Ayer
,
J.
(
2018
)
1: 2 000 000 scale geological compilation of the Superior Craton–version 1. Mineral Exploration Research Centre
,
Harquail School of Earth Sciences
, Laurentian University Document Number MERC-ME-2018-017.
Google Scholar

30.
Moreira
,
H.
,
Storey
,
C.
,
Bruand
,
E.
,
Darling
,
J.
,
Fowler
,
M.
,
Cotte
,
M.

,
Villalobos-Portillo
,
E.E.
,
Parat
,
F.
,
Seixas
,
L.
,
Philippot
,
P.
, and others. (
2023
)
Sub-arc mantle fugacity shifted by sediment recycling across the Great Oxidation Event
.
Nature Geoscience
,
16
,
922
–
927
, https://doi.org/10.1038/s41561-023-01258-4.
Google Scholar
Crossref

31.
Moyen
,
J.F.
(
2009
)
High Sr/Y and La/Yb ratios: The meaning of the “adakitic signature.”
Lithos
,
112

, 556 – 574 , https://doi.org/10.1016/j.lithos.2009.04.001.
Google Scholar
Crossref

32. Moyen , J.F. and van Hunen , J. (2012) Short-term episodicity of Archaean plate tectonics . *Geology* , 40 , 451 – 454 , https://doi.org/10.1130/G322894.1.
GeoScienceWorld
Google Scholar
Crossref

33. Parat , F. and Holtz , F. (

2004
)
Sulfur partitioning between apatite and melt and effect of sulfur on apatite solubility at oxidizing conditions
.
Contributions to Mineralogy and Petrology
,
147
,
201
–
212
, https://doi.org/10.1007/s00410-004-0553-7.
Google Scholar
Crossref

34.
Percival
,
J.A.
(
2007
) Geology and metallogeny of the Superior Province, Canada. In
W.D.
Goodfellow
, Ed.,
Mineral deposits of Canada: A synthesis of major deposit-types, district metallogeny, the evolution of geological provinces, and exploration methods
, p.
903
–
928
.
Geological Association of Canada, Mineral Deposits Division
. Special Publication No. 5.

35.
Piccoli
,
P.M.
and
Candela
,

P.A. (2002) Apatite in igneous systems. *Phosphates: Geochemical, Geobiological, and Materials Importance*, 48, 255–292.
Google Scholar

36. Richards, J.P. (2011) Magmatic to hydrothermal metal fluxes in convergent and collided margins. *Ore Geology Reviews*, 40, 1–26, https://doi.org/10.1016/j.oregeorev.2011.05.006.
Google Scholar
Crossref

37. ——— (2015) The oxidation state, and sulfur and Cu contents of arc magmas: Implications for metallogeny.

Lithos, 233, 27–45, https://doi.org/10.1016/j.lithos.2014.12.011.
Crossref

38. Sadove, G., Konecke, B.A., Fiege, A., and Simon, A.C. (2019) Structurally bound S^{2-}, S^{1-}, S^{4+}, S^{6+} in terrestrial apatite: The redox evolution of hydrothermal fluids at the Phillips mine, New York, USA. *Ore Geology Reviews*, 107, 1084–1096, https://doi.org/10.1016/j.oregeorev.2019.03.033.
Google Scholar
Crossref

39. Sillitoe, R.H. (2010) Porphyry copper systems. *Economic Geology and the Bulletin of the Society of Economic Geologists*, 105, 3–41, https://doi.org/10.2113/gsecongeo.105.1.3.
GeoScienceWorld
Google Scholar
Crossref

40. Sizova, E., Gerya, T., Brown, M., and Perchuk, L.L. (2010) Subduction styles in the Precambrian: Insight from numerical experiments.

Lithos
,
116
,
209
–
229
, https://doi.org/10.1016/j.lithos.2009.05.028.
Google Scholar
Crossref

41.
Tang
,
M.
,
Erdman
,
M.
,
Eldridge
,
G.
, and
Lee
,
C.T.A
. (
2018
)
The redox “filter” beneath magmatic orogens and the formation of continental crust
.
Science Advances
,
4
(
5
), eaar4444.
Google Scholar

42.
Tassara
,

S.
,
Reich
,
M.
,
Konecke
,
B.A.
,
González-Jiménez
,
J.M.
,
Simon
,
A.C.
,
Morata
,
D.
,
Barra
,
F.
,
Fiege
,
A.
,
Schilling
,
M.E.
, and
Corgne
,
A.
 (
2020
)
Unravelling the effects of melt-mantle interactions on the gold fertility of magmas
.
Frontiers in Earth Science
 ,

8
,
29
, https://doi.org/10.3389/feart.2020.00029.
Google Scholar
Crossref

43.
Thurston
,
P.C.
,
Ayer
,
J.A.
,
Goutier
,
J.
, and
Hamilton
,
M.A.
(
2008
)
Depositional gaps in Abitibi Greenstone Belt stratigraphy: A key to exploration for syngenetic mineralization
.
Economic Geology and the Bulletin of the Society of Economic Geologists
,
103
,
1097
–
1134
, https://doi.org/10.2113/gsecongeo.103.6.1097.
GeoScienceWorld
Google Scholar
Crossref

44.

Tollan, P. and Hermann, J. (2019) Arc magmas oxidised by water dissociation and hydrogen incorporation in orthopyroxene. *Nature Geoscience*, 12, 667–671, https://doi.org/10.1038/s41561-019-0411-x.
Google Scholar
Crossref
PubMed

45. Ulmer, P., Kaegi, R., and Müntener, O. (2018) Experimentally derived intermediate to silica-rich arc magmas by fractional and equilibrium crystallization at 1.0 GPa: An evaluation of phase relationships, compositions, liquid lines of descent and oxygen fugacity.

Journal of Petrology, 59, 11–58, https://doi.org/10.1093/petrology/egy017.
Google Scholar
Crossref

46. Valley, J.W., Kinny, P.D., Schulze, D.J., and Spicuzza, M.J. (1998) Zircon megacrysts from kimberlite: Oxygen isotope variability among mantle melts. *Contributions to Mineralogy and Petrology*, 133, 1–11, https://doi.org/10.1007/s004100050432.
Google Scholar
Crossref

47. Wyman, D. and Kerrich, R. (2009) Plume and arc magmatism in the Abitibi subprovince: Implications for the origin of Archean continental lithospheric mantle. *Precambrian Research*, 168, 4–22, https://doi.org/10.1016/j.precamres.2008.07.008.
Google Scholar
Crossref

Supplementary data

9387_supp- pdf file
9387_supp1- xlsx file
9387_supp2- xlsx file
9387_supp3- xlsx file
9387_supp4- xlsx file
9387_supp5- xlsx file